33RD CONGRESS
OF THE INTERNATIONAL COUNCIL
OF THE AERONAUTICAL SCIENCES
STOCKHOLM, SWEDEN, 4–9 SEPTEMBER, 2022

ICAS
2022
SWEDEN

LATTICE BOLTZMANN METHOD FOR BROADBAND NOISE PREDICTIONS ON A TURBULENCE-CASCADE TEST RIG INCLUDING SERRATED VANES

Martin Buszyk[1], Lucien Vienne[2], Thomas Le Garrec[1], Jean-François Boussuge[2], Cyril Polacsek[1] & Raphaël Barrier[1]

[1]DAAA, ONERA, Université Paris Saclay F-92322 Châtillon - France
[2]CERFACS - Centre Européen de Recherche et de Formation Avancée en Calcul Scientifique, 31100 Toulouse - France

Abstract

In order to reduce rotor-stator interaction noise on future high-bypass engines, silent Outlet Guided Vanes (OGVs) have to be designed. This study focuses on noise predictions by means of weakly compressible and compressible lattice Boltzmann simulations, along with aerodynamic assessment. Computations are performed on a full test rig including a grid generated turbulence interacting with a seven vanes rectilinear cascade as in the test campaigns at Ecole Centrale de Lyon. Moreover, the noise reduction achieved by two passive treatments proposed by Onera, which are based on leading edge serrations, is evaluated.

Keywords: lattice Boltzmann method, aeroacoustics, turbulence-cascade interaction, serrations

1. Introduction to the study and context of the project

With the continuous growth of air traffic and the tightening of new airport noise restrictions, the reduction of the noise radiated by turbofan engines requires innovative solutions. Modern engines now reach very high by-pass ratios, significantly decreasing fuel consumption. But, with limited space between the rotor and stator, fan - Outlet Guided Vane (OGV) interaction noise becomes at present a dominant source at low Mach regimes. The European project InnoSTAT (innovative stator, https://cordis.europa.eu/project/id/865007) addresses this challenge by assessing experimentally and numerically several low-noise OGV concepts. These concepts proposed by the consortium partners are tested in a simplified rectilinear cascade configuration at Ecole Centrale de Lyon, illustrated in Figure 1, which is presented in the next section.
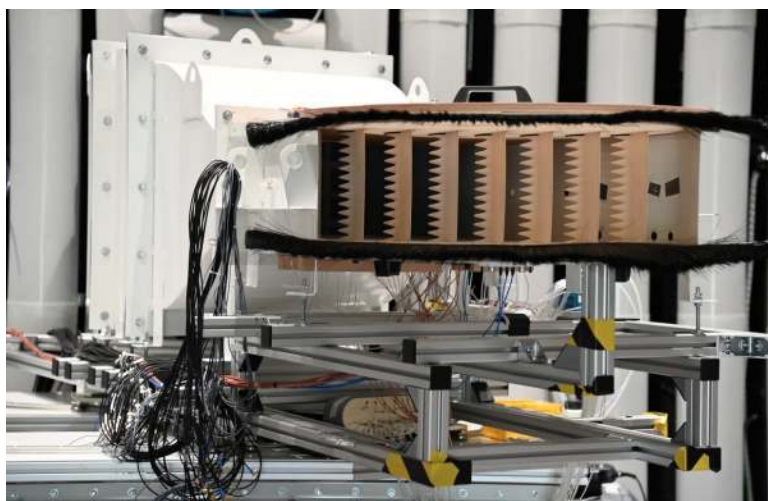

Figure 1 – Picture of the test-rig at ECL during the InnoSTAT test campaign.

One particular acoustic treatment proposed by ONERA is the serrated leading edge [1, 2, 3, 4, 5], it aims at reducing turbulence-airfoil interaction noise. The design of the serrations was defined in previous works [6, 7]. Indeed, in order to define and roughly validate the low-noise designs, preliminary analytical and numerical solutions have already been provided [7, 8]. They consisted in Reynolds Averaged Navier-Stokes (RANS) computations for aerodynamic behaviour [7] and analytical and Computational AeroAcoustics (CAA) calculations for the acoustic predictions [6, 7], and along with preliminary lattice Boltzmann (LBM) results. It has to be noted that these first LBM computations, restricted to weakly compressible flows, have been already performed in [8], but, with a coarser mesh around the NACA profiles and in the acoustic region, than the set-up presented here. Two geometries have been proposed, which are illustrated in Figure 2. The second one featuring the same leading edge pattern than the first one but with an increased mean chord allowing for better aerodynamic performances in terms of pressure loss coefficient and remaining swirl at the outlet. Please refer to [7] for more information.
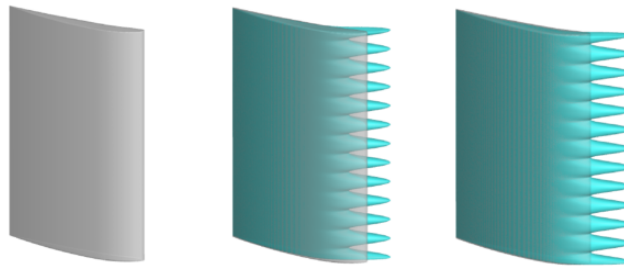

Figure 2 – Baseline NACA7310 in grey, serrated $d1$ (b), serrated $d2$ (c).

The purpose of this study is to focus on recent high fidelity simulations performed by ONERA and CERFACS employing the lattice Boltzmann method by means of the ProLB solver [9]. Contrary to the traditional CFD solver based on Navier-Stokes equations, the lattice Boltzmann method (LBM) originates from the kinetic theory of gases. Since only the macroscopic behaviour of the fluid is needed, a simplified kinetic equation has to be solved. The resulting algorithm executes efficiently on parallel computers and offers a very low numerical dissipation. Moreover, immersed boundary conditions handle with ease complex geometries. For all these reasons, the ProLB software is a good candidate for simulating challenging aeroacoustics configurations. ProLB has successfully computed a ducted fan combined with a a turbulence grid [10] and recently applied on the NASA ANCF turbofan benchmark case [11]. Another LBM solver has also been favourably used to perform simulations on leading edge serrations [12, 13]. The main contribution of the direct LBM simulations with ProLB is to take into account almost the complete test installation, as illustrated in Sections 2, 4. Simulations are performed with weakly compressible and compressible versions of ProLB solver, presented in section 3. A first calculation has been carried out at the approach condition (APP) at M=0.34 (measured half a chord in front of the cascade) with the weakly compressible version of the solver. However, the weakly compressible version was not able to perform the computation at M=0.53 corresponding to the cutback condition (CUTB). Indeed, locally the Mach number exceeded M=0.7, which is the limit for weakly compressible simulations. In order to simulate the flow at the cutback condition, a compressible version of the code has been used by Cerfacs. It allows to numerically assess the acoustic performances of the low-noise designs at highest speed (CUTB).

The paper is organised as follows:

1. The experimental set-up which is simulated is presented in section 2.

2. Section 3 details the main features of the LBM solver proLB used for the simulations. Differences between the weakly compressible and compressible approaches are highlighted.

3. The geometries and main numerical parameters of the simulations are provided in section 4.

4. In section 5, the aerodynamic performance of the treated NACA airfoils are discussed in comparison with the reference profile, in terms of mean flown, forces, and Cp profiles. Two oper-

ating points are investigated, one that fits the approach condition (APP) at M=0.34 and one the cutback condition (CUTB) at M=0.53. A comparison with reference RANS calculations is performed for the two operating points.

5. The turbulence grid properties is analysed in section 6, especially in terms of turbulence intensity and integral length scale.

6. Acoustic analyses are performed in section 7, in terms of pressure sources at the vane skin and far-field propagation. Direct noise calculations are complemented by a coupling with an integral method based on the Ffowcs Williams and Hawkings (FWH) equation in solid formulation (using turbulent pressure on vane surfaces as input data).

7. In the conclusion, capabilities and issues of the investigated LBM setups (weak or full compressible simulations) regarding to aerodynamics and acoustics are pointed out.

Remarks The present paper comes along with a companion paper to ICAS 2022 [14], which is focused on comparison with experimental results in terms of aerodynamics and acoustics.

2. Presentation of the experimental test-rig

The test facility used in the first test campaign of the InnoSTAT project is presented in Figure 3. It consists of seven evenly spaced NACA7310 airfoils, which are mounted on a rotating disk to modify the cascade angle. The NACA profiles are impinged by a turbulent inflow, which is generated by a grid placed in the test section upstream of the nozzle. The nozzle accelerates the flow by a geometrical squeezing in order to reach the adequate mean flow of 120 m/s and 180 m/s (corresponding to a Mach number of 0.34 and 0.53). The main parameters relevant to the simulations are given in Table 1.
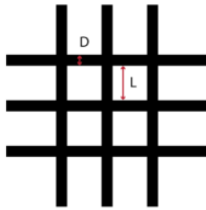
	Parameter	Value
Airfoil	shape	NACA7310
	chord c	12 cm
	span L_z	20 cm
	inter-vane space s	8.5 cm
Upstream flow	Mach number (**U** direction)	0.34 and 0.53
	Angle between cascade and flow axis	34°
Turbulence grid		Rectangular section: D = 1 cm L = 4 cm

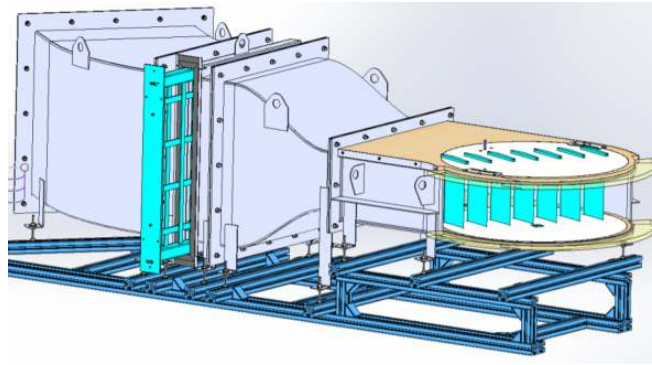Table 1 – Main parameters of the rectilinear cascade test-rig.

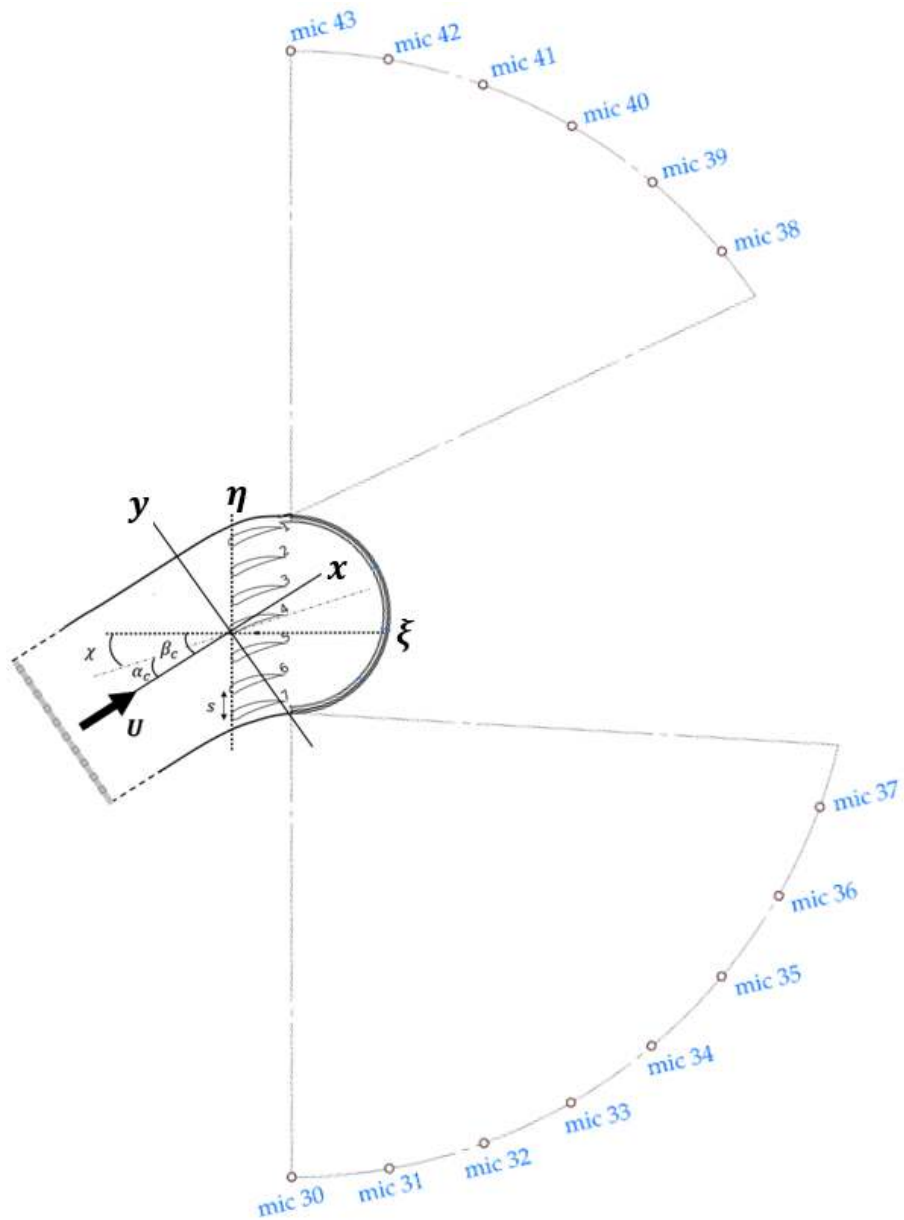Figure 3 – 3D scheme of the test facility for InnoSTAT at ECL

Figure 4 – 2D sketch of the test geometry in the cascade frame and far-field microphone antenna.

As for the measurements, 1D and 2D hot wire anemometers are used to quantify the upstream mean flow, turbulence, and boundary layer, along with pressure tubes extending in the width of the test section in order to check the homogeneity of the flow. The wake behind airfoils is characterized by 1D hot wires. Probes are also placed on the central vane to monitor the pressure at the vane

skin, and provide among others Cp profiles. Finally, main acoustic measurement consists of an 14-microphones circular antenna placed at radius 1.95 m of the central vane, as illustrated by Figure 4. An axial array is also placed inside of the test section to perform in-duct acoustic measurements upstream of the cascade. It has to be noted that more information, concerning the experimental set-up and instrumentation, is provided in another submission [14] to ICAS 2022, which is dedicated to the comparison between experimental data and predictive methods (analytical and numerical solutions: CAA, RANS, and LBM).

3. Overview of the lattice Boltzmann ProLB solver

LBM simulations are carried out by means of the ProLB solver. It has been developed by a French consortium composed of universities, research institutes and industries (CS group, Airbus, Renault, École Centrale de Lyon, and Aix Marseille Université) [1]. The main variable in the lattice Boltzmann method is the distribution function, from which the density and momentum of the fluid are given by its statistical moments. The discrete distribution function involves nineteen components, also called D3Q19, that propagate and collide along the different sites of a Cartesian lattice. To enhance the stability and robustness of the scheme, the solver features an advanced collision model, the hybrid recursive regularized operator [15]. Equally important, this collision operator combined with a grid refinement transition algorithm reduces significantly spurious noises [16, 17]. Similarly to traditional CFD solvers, a large eddy simulation turbulence model controls the unresolved turbulent dynamics. In the present case, the shear-improved Smagorinsky model (SISM) [18] is employed as a subgrid-scale viscosity to model unresolved small-size eddies. Solid surfaces are defined by immersed boundary conditions, where the fluid boundary layer is modeled by a wall log-law with corrections to take into account the adverse longitudinal pressure gradient and the curvature at the boundary.

At the origin, the lattice Boltzmann method was restricted to the weakly compressible regime. Persistent developments have made it possible to simulate compressible flows, greatly extending the range of applications. The present compressible lattice Boltzmann method introduces an entropy equation solved by a finite difference method [19, 20]. The use of a segregated numerical solver for the lattice Boltzmann and entropy equations enables the simulation of compressible flows on a broad range of Mach numbers.

4. Numerical configurations

The numerical setups modeling the experimental test-rig introduced in section 2 are presented here. Simulations are carried out approximately at the approach APP operating point (M=0.34) with both the weakly-compressible and compressible versions of the solver and at the cutback CUTB condition (M=0.53) with the compressible version of the solver only.

The Figures 5a and 5b show the geometry from the graphical user interface of the ProLB software. The test section is represented with the nozzle and the grid, along with the seven vanes cascade (here depicted with the leading edge serrations).

---

[1]http://www.prolb-cfd.com/

(a)   (b)
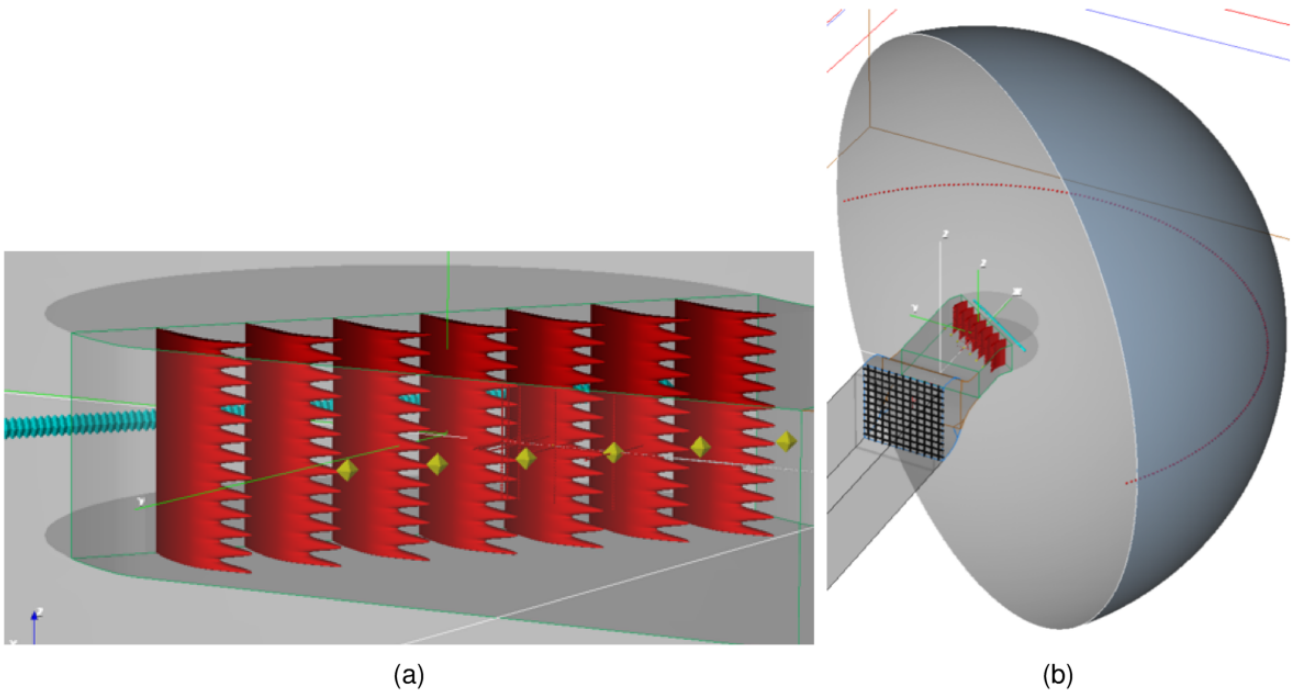
Figure 5 – View of the cascade geometry with serrations (a). View of the test rig geometry (b).

An illustration of the octree mesh close to the leading-edge is presented in Figure 6. Two successive layers of fine mesh protect the airfoil's geometry.
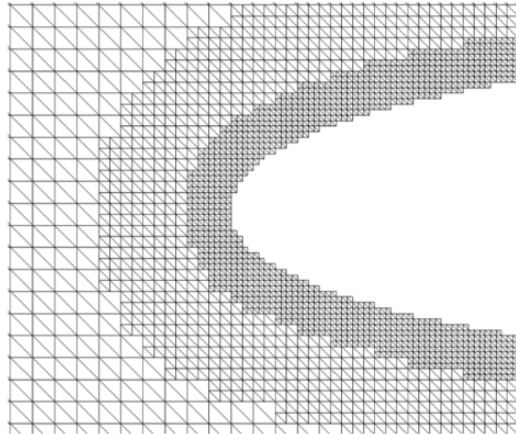

Figure 6 – Octree mesh near the NACA leading edge.

The Table 2 provides an overview of the different LBM simulations, depending on the version of the ProLB solver (weakly compressible and compressible) and the inflow Mach number. The simulation set-up between the LBM weakly compressible and compressible runs are not exactly the same due to some limitations in the computational resources.

Inflow Mach number	M=0.34		M=0.53
Geometries	baseline, serrated $d1$, serrated $d2$		
Version of the code	weakly compressible	compressible	compressible
Simulation time	≈ 0.404 s	≈ 0.3s	≈ 0.3s
dx_{min} (around NACA airfoils)	0.2 mm	0.3 mm	0.3 mm
Time step	≈ 3.4 ×10^{-7}	≈ 2.7 ×10^{-7}	≈ 2.7 ×10^{-7}
Number of iterations	1.2 million	1.1 million	1.1 million

Table 2 – Lattice Boltzmann simulations setups, for both baseline and serrated geometries.

6

Several outputs are included in order to post process the computations, which include among others: surface outputs on the vane skin and grid, and various point probes both in the test section to assess mean flow and turbulence properties and in the far-field to evaluate noise radiation. As detailed later in the section 7, apart from the direct acoustic computations extracted from probes corresponding to the microphone antenna in the test campaign (see Figure 4), indirect noise calculations are also performed. They consist in the extraction of wall pressure on the vane skin and radiation in the far-field by solving Ffowcs Williams-Hawkings integral in the frequency domain in solid formulation (MIA in-house ONERA code for the weakly compressible computations).

5. Aerodynamic behaviour of the reference and low-noise designs

The post-treatments presented here and in the section 7 are done after a transient time: 0.2 s for the computations at M=0.34 and 0.17 s for the computations at M=0.53. Preliminary convergence studies were performed in [8]. First, a comparison between LBM simulations and reference RANS calculations is performed. It has to be noted that the RANS computations consist in a 1-vane computation with periodic boundary conditions (see [7] fore more details). In spite of that, a very good agreement can be observed between the two solutions in terms of pressure coefficient profiles, Cp, as illustrated in Figure 7 for the baseline geometry. For the LBM simulations, the pressure has been extracted at mid-span from the central vane. Small oscillations on the suction side are visible on the LBM results. In this region, large curvature induces steep geometrical variations of the octree mesh, which may produce some oscillations in the boundary solution.
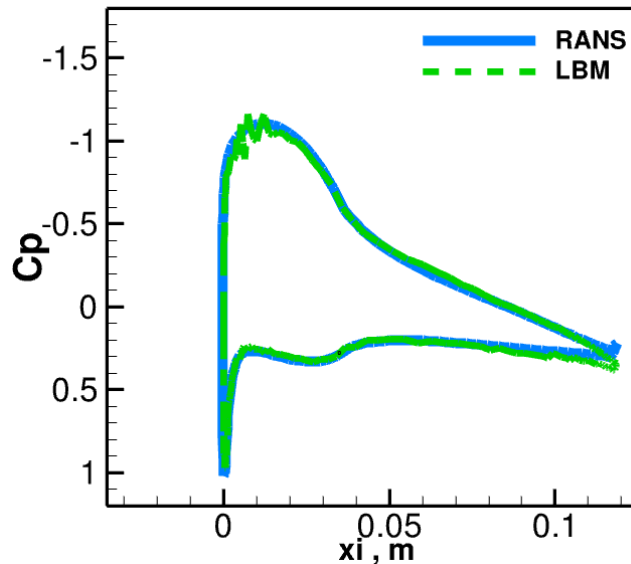

Figure 7 – Cp profile of the central vane at midspan for the baseline configuration (weakly compressible version) at M=0.34.
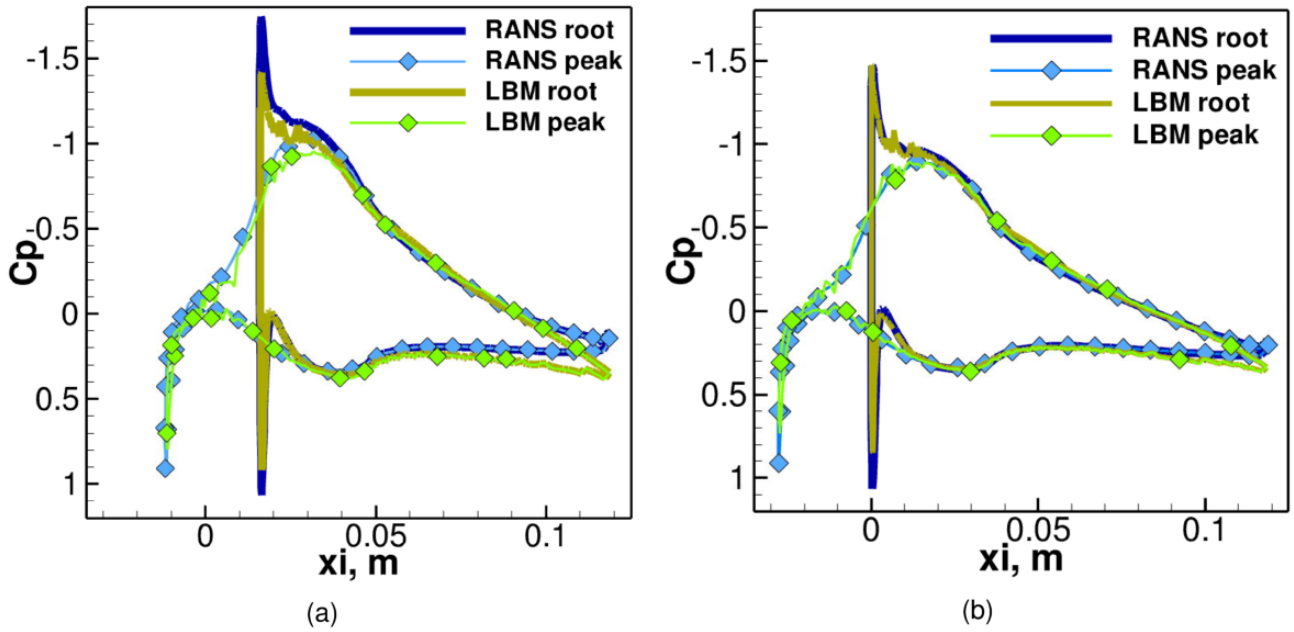
Figure 8 – Cp profile of the central vane at midspan for the serrated $d1$ (a) and $d2$ (b) configurations (weakly compressible version) at M=0.34.

The Cp profiles for the serrated geometries $d1$ and $d2$ are illustrated in Figure 8. The mean pressure has been extracted at peak and root locations around mid-span. Again, a good agreement appears with the RANS solutions, even if larger difference can be observed near the trailing edge in particular for the $d1$ calculation.

A very good agreement is also observed between RANS calculation at M=0.53 and LBM computations for the reference design with the compressible version of the solver as illustrated in Figure 9. As for M=0.34, the shape of the pressure coefficient profile is very similar for serrated designs $d1$ and $d2$.
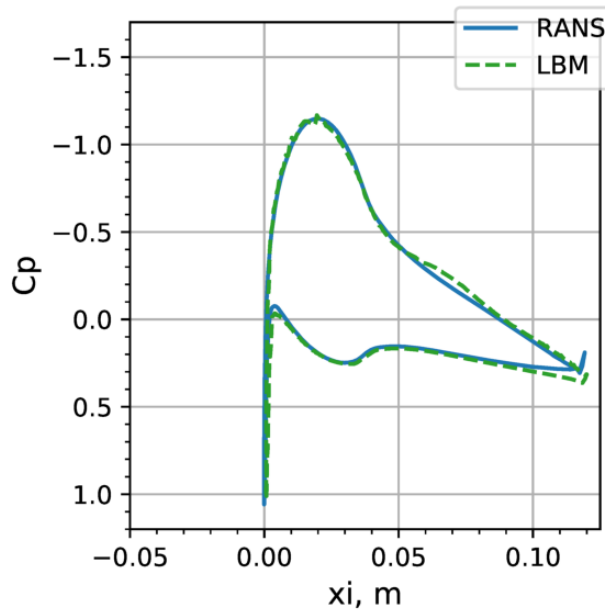

Figure 9 – Cp profile of the central vane at midspan for the baseline configuration (compressible version) at M=0.53.
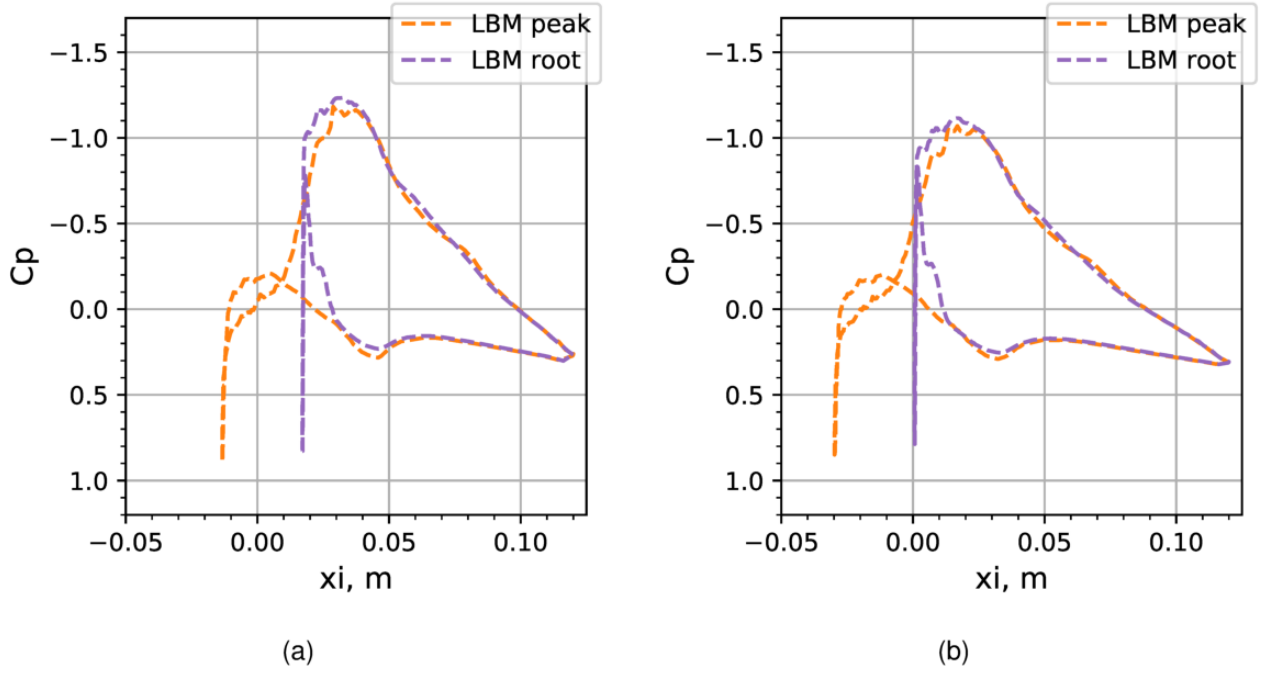
(a)   (b)

Figure 10 – Cp profile of the central vane at midspan for the serrated $d1$ (a) and $d2$ (b) configurations (compressible version) at M=0.53.

In terms of aerodynamic load, forces are also compared in Table 3 for the two inflows (M=0.34 and M=0.53) with the compressible version of the solver.

geometry	F_x [N]		F_y [N]	
	Ma=0.34	Ma=0.53	Ma=0.34	Ma=0.53
baseline	26.12	66.18	102.74	263.51
serrated $d1$	24.51	63.21	92.35	235.02
serrated $d2$	26.03	64.09	101.33	254.71

Table 3 – Average loads on the central vane in the test section coordinate system (x axis aligned with the test section). Calculation performed with the compressible version of the code.

From Table 3, one can deduce that forces are roughly multiplied by a factor 2.43 (corresponding to the ratio of the squared Mach number). Moreover, far closer results to the reference baseline geometry are obtained with the second design $d2$ because of the longer mean chord compared to design $d1$. A detailed analysis of the profiles in terms of aerodynamic penalties (pressure loss coefficient and remaining swirl) has been performed in [7] by means of RANS calculations.

6. Turbulent grid flow analyses

Analysis of turbulence properties is of prime importance for serration design (see [7] for $d1$ and $d2$ definition). The Figure 11 illustrates the instantaneous fluctuating velocity field in the mid-planes of the test section.
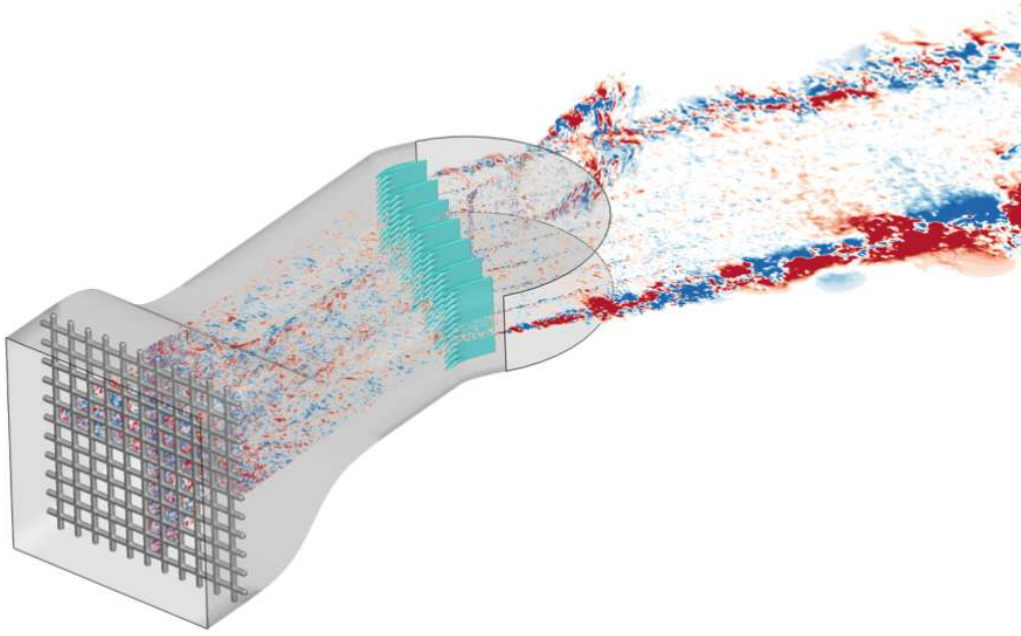
Figure 11 – Snapshot of the fluctuating velocity at plane $y = 0$ and $z = 0$ (weakly compressible calculation)

The fluctuating velocity field generated by the grid is clearly visible in Figure 11. Turbulent wakes generated by lateral plates at the exit of the test section are also reproduced.

Turbulence properties generated by the grid can be computed from a line of point probes placed in the middle of the section. The coordinate system is illustrated in Figure 4. First, turbulence intensity (TI) can be computed as follows:

$$\text{TI} = \frac{\sqrt{\frac{1}{3}\left(u_x'^2 + u_y'^2 + u_z'^2\right)}}{U} \tag{1}$$

The ratio of the velocity fluctuations to mean flow field can also be defined separately for each direction:

$$\begin{cases} \text{TI}_x = \dfrac{\sqrt{u_x'^2}}{U} \\[2ex] \text{TI}_y = \dfrac{\sqrt{u_y'^2}}{U} \\[2ex] \text{TI}_z = \dfrac{\sqrt{u_z'^2}}{U} \end{cases} \tag{2}$$

Secondly, the longitudinal turbulent length scale can also be obtained from spatial correlations along the axial direction:

$$L_l = L_{xx,x} = 2\int_0^{+\infty} \frac{u_x'(\mathbf{X}-\mathbf{l_x},t)u_x'(\mathbf{X}+\mathbf{l_x},t)}{\sqrt{u_x'(\mathbf{X}-\mathbf{l_x},t)^2}\sqrt{u_x'(\mathbf{X}+\mathbf{l_x},t)^2}}\mathrm{d}l_x \tag{3}$$

The Figure 12 shows the evolution of the turbulence intensity between the grid and the leading edge of the vanes.
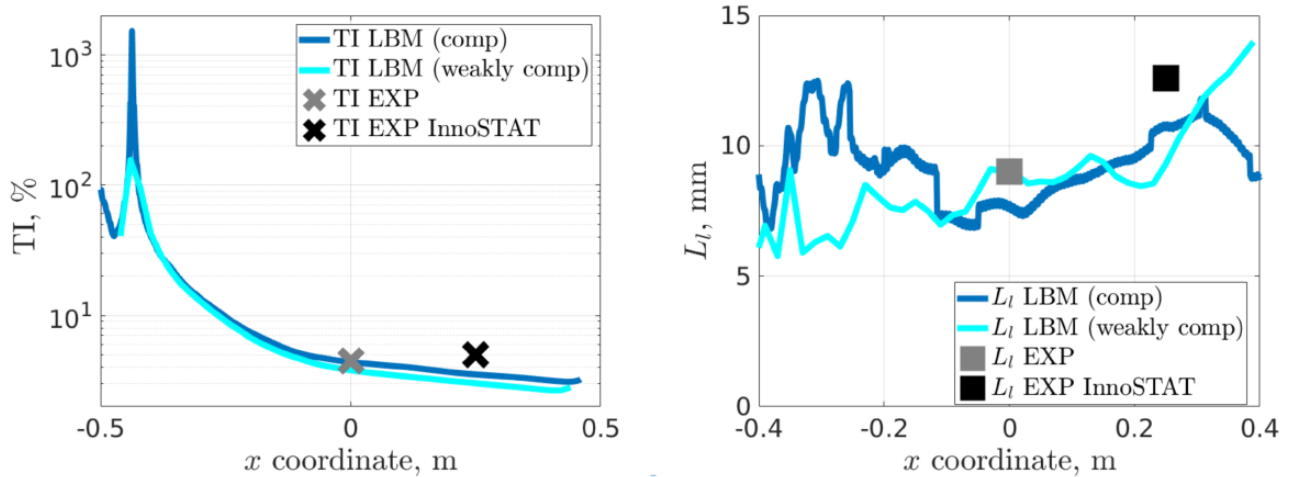
Figure 12 – Turbulence grid properties (intensity and length scale) (at M=0.34).

One may observed that there is a rather good agreement with the experimental data from a previous experimental data (in grey), which has been calculated using a smaller test section (please refer to [5] for additional details). A rather good agreement is also observed between the weakly compressible and compressible simulations. Indeed, it has to be reminded that different setups have been used by the project partners. Moreover, the integral correlations are far more sensitive to post-process than the turbulence intensity. As for the experimental values from the InnoSTAT test campaign, values were obtained at an inflow of 95 m/s, which is a bit slower that the inflow condition of the numerical computations. There is a larger difference with the numerical results in terms of turbulence intensity and length scale with these values. It might be due to the grid manufacturing. Indeed, the inflow speed is not expected to influence much the turbulent intensity and length scale, as described for example in [21]. The latter point is also addressed below through comparison between turbulence properties at M=0.34 and M=0.53.

Turbulence intensity has been also computed for the the two inflow conditions at M=0.34 and M=0.53 using the compressible version of the solver.
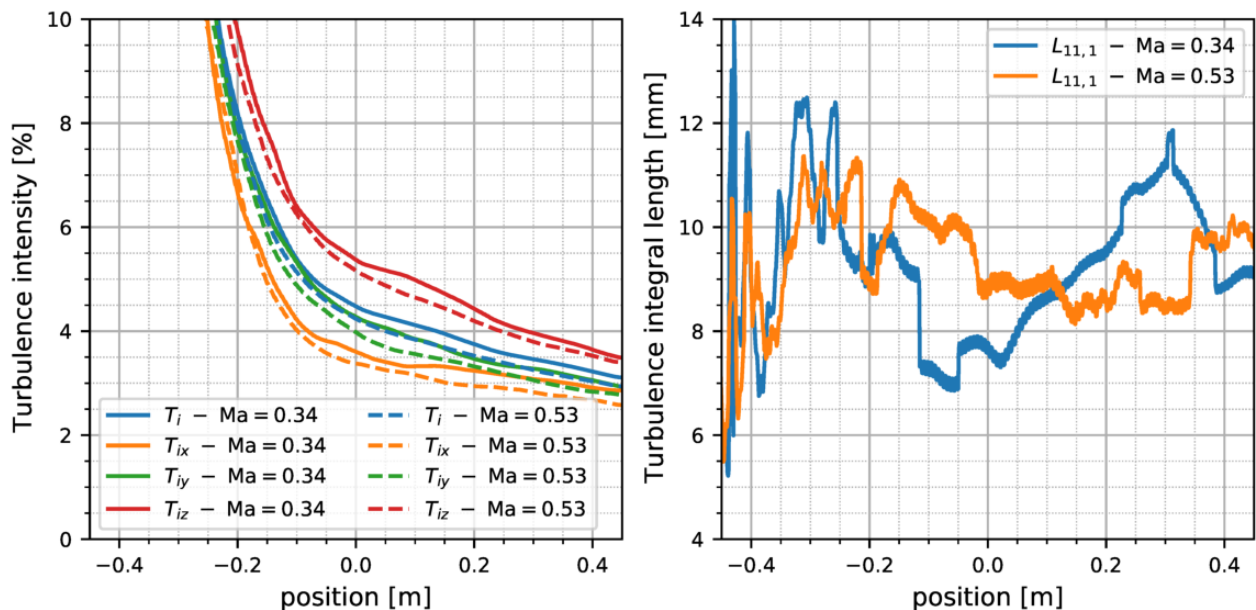

Figure 13 – Turbulence intensity and integral length scale obtained with the compressible version at M=0.34 and M=0.53.

It is interesting to note from Figure 13 (a), that turbulence is not perfectly isotropic. The strongest component is on the z the axis, which might due to the strong contraction of the nozzle along this direction (as illustrated in Figure 3). Moreover, turbulent intensity only marginally evolves when the velocity increases. As for turbulent length scale, again from Figure 13, a value of roughly 10 mm is recovered.

7. Noise sources and far-field propagation

The acoustic field primarily generated by the interaction between the turbulence grid and NACA airfoils is now analysed. The Figure 14 illustrates a snapshot the fluctuating pressure in the plane $z = 0$. Acoustic waves are clearly visible in the domain, outside of the hydrodynamic wake.
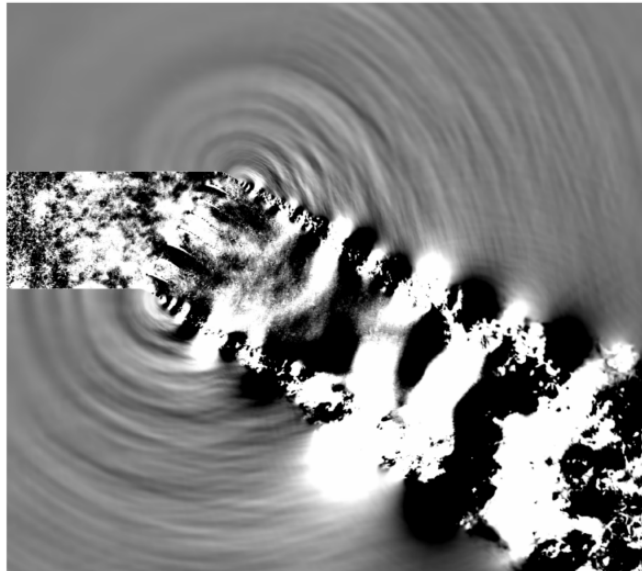

Figure 14 – Visualization of the fluctuating pressure (p', levels between ± 20 Pa) at mid-span in the simulation domain - M=0.34 (weakly compressible calculation).

In order to have a first overview of the acoustic sources, the fluctuating pressure sources have been extracted at the vane skin. The root mean square (RMS) fluctuating pressure (p'_{RMS}) distribution is illustrated in Figures 15a and 15b at M=0.34 (weakly compressible version of the solver). Two major areas of fluctuating pressure are visible on the baseline geometry. A primary area of high pressure fluctuations is located at the leading edge and is caused by dipolar noise sources from the turbulence-airfoil interaction noise. A secondary high pressure fluctuation band is noticeable near the mid chord due to the turbulent boundary layer transition. These two locations of the noise sources are also observed in the work of Lewis [22] (see pages 140-141, in particular). As expected from the literature [23, 24, 7], the leading edge pressure sources are concentrated at the roots and tips of the serrations in the low noise design configurations (see Figure 15b). The shape of the secondary noise source is also modified by the presence of serrations. This source, due to the turbulent boundary layer, is expected to reduce the efficiency of the leading edge treatment [22].
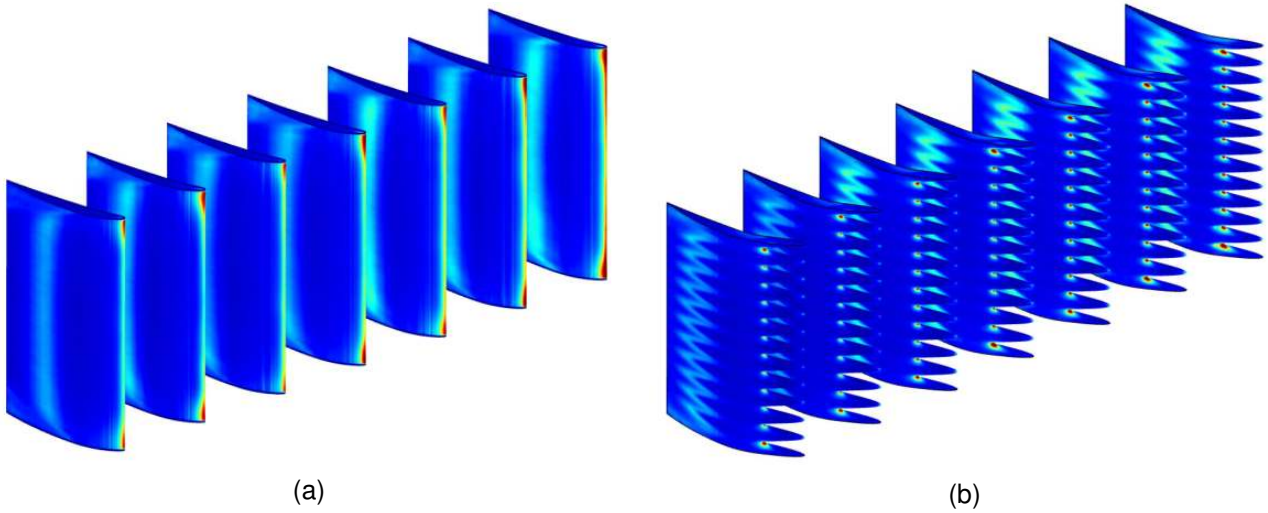
(a)
(b)

Figure 15 − p'_{RMS} on the vane skin (levels between 0 and 1000 Pa). Weakly compressible calculations on the baseline (a) and serrated $d1$ (b) geometries.

We now briefly compare the weakly-compressible and compressible simulations at M=0.34 using Figures 15a, 15b and 16. We observe that the noise sources are a slightly stronger in the suction area for the compressible simulations. We relate this effect to the coarser mesh employed ($c/dx_{min} = 400$) compare to the weakly compressible computations ($c/dx_{min} = 600$).
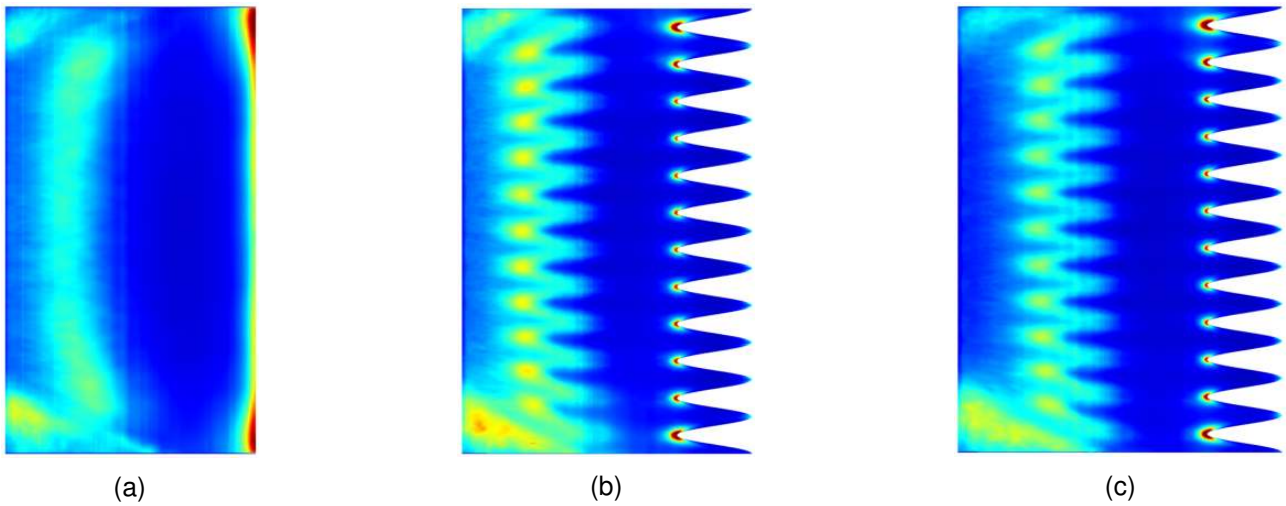

(a)
(b)
(c)

Figure 16 − p'_{RMS} on the vane skin (levels between 0 and 1000 Pa). Compressible calculations on the baseline (a), serrated $d1$ (b) and serrated $d2$ (c) geometries - M=0.34.
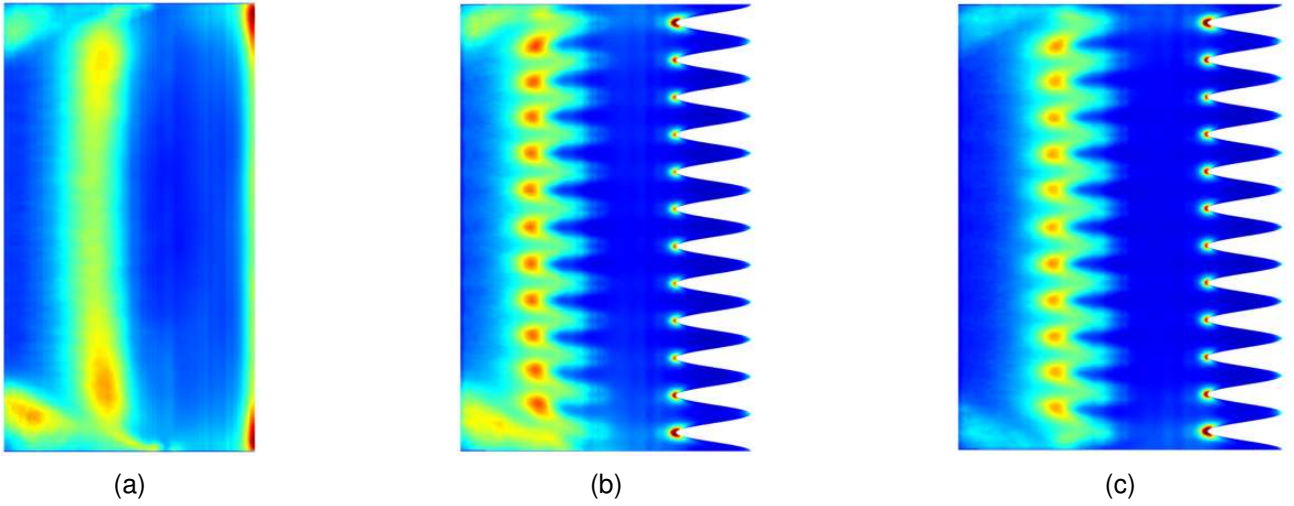
(a) (b) (c)

Figure 17 – p'_{RMS} on the vane skin (levels between 0 and 2500 Pa). Compressible calculations on the baseline (a), serrated $d1$ (b) and serrated $d2$ (c) geometries - M=0.53.

Using Figures 16 and 17, we highlight the effect of the Mach number. As it can be expected, when the mean flow velocity is increased, the pressure sources are much stronger. It has to be noted that the color-map range is larger for the M=0.53 configuration. Moreover, the difference between the leading edge and turbulent boundary layer pressure sources is smaller in the M=0.53 case. It might decrease the acoustic performance of the leading edge treatment. Again, these sources are weaker with the design $d2$ in comparison with design $d1$, for both inflows illustrated in Figures 16 and 17.

With the serrated $d1$ design, the turbulent boundary layer sources are stronger since the minimum chord (located at the roots) is smaller with this design. Indeed, the $d1$ design presents a larger turbulent boundary layer than the baseline geometry (as shown by RANS calculations in [7]). With the aerodynamically improved design $d2$, the sources are weaker. Indeed, the shape of the airfoil at the roots of the serrations corresponds to the baseline geometry, which facilitates the flow deviation by the cascade. The reader may also notice a large asymmetry on the pressure fluctuations along the span due to differences in the corner separation flows. This phenomenon is accentuated by the use of a mesh that is not exactly symmetric in the span-wise direction. This issue was corrected for serrated $d2$ calculation at M=0.53 (Figure 17c).

An assessment in terms of far-field noise reduction is also achieved. A first solution consists in the extraction of the pressure sources at the vane skin and performing a Ffowcs Williams-Hawkings (FWH) integral method. The calculation is carried out by means of MIA (an in-house ONERA code) in the frequency domain, considering the FWH in solid formulation with a free-field Green function. A second solution, more straightforward, consists in computing acoustic spectra directly from probes placed at the microphone location (see Figure 4). To perform the calculation, it is of prime importance, as in the experimental set-up to exclude data from the hydrodynamic wake, which would otherwise pollute the spectra in particular in the low frequency range. Moreover, in order to get a general view of the noise reduction, an angular integration of the acoustic Power Spectral Density (PSD) spectra (avoiding the hydrodynamic wake) is performed following (due to the log functions difference, the surface of integration disappears):

$$\Delta\text{PWL} = 10\log_{10}\left(\sum_{mics}\text{PSD}_{\text{baseline}}\right) - 10\log_{10}\left(\sum_{mics}\text{PSD}_{\text{serrated}}\right) \tag{4}$$
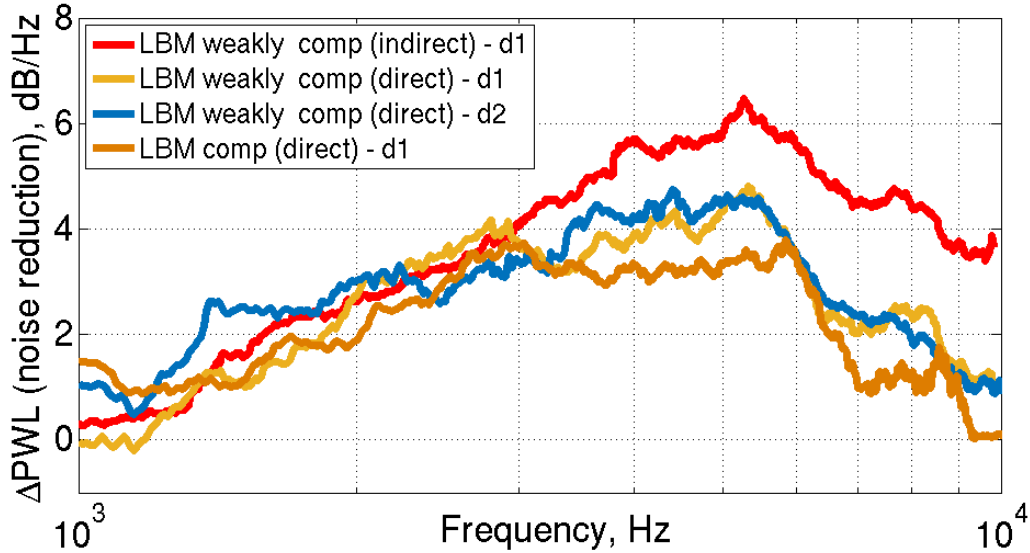
Figure 18 – Noise reduction assessment at the approach condition (M=0.34)

The Figure 18 shows noise reductions obtained at M=0.34. Results are consistent in the low and medium frequency range. However, a larger noise reduction is observed with the indirect calculation (FWH analogy). Indeed, only the noise sources at the vanes surfaces are radiated in the far-field: any other sources present in the test-rig can not be properly taken into account. Serrated designs $d1$ and $d2$ provide a very similar noise reduction, which reinforces the interest of the second design improved from the aerodynamic point of view [7]. With the compressible calculation noise reduction is very similar apart small differences due to slightly different set-up between the weakly compressible and compressible simulations.
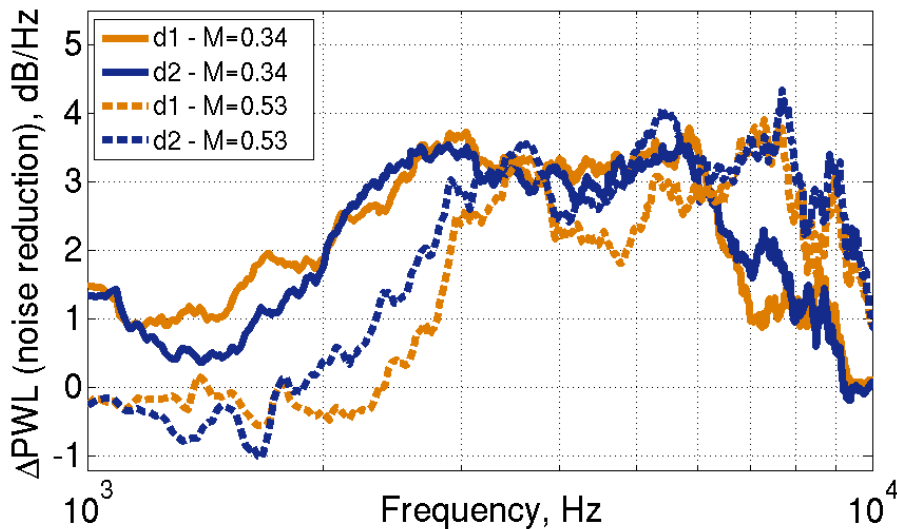

Figure 19 – Comparison of the noise reduction obtained with $d1$ and $d2$ at M=0.34 and M=0.53 (direct compressible calculations).

The Figure shows the noise reduction obtained from design $d1$ and $d2$ at M=0.34 and M=0.53. A similar trend is observed between $d1$ and $d2$, which again favours the choice of the second design for turbofan application since it provides a huge improvement in terms of aerodynamic penalties (please refer to [7] for detailed RANS evaluations). When the inflow speed is increased, the noise reduction is shifted towards high frequencies, which is consistent with the literature [23, 2, 3].

8. Concluding remarks

High fidelity lattice Boltzmann simulations have been carried out on the full test-rig of the InnoSTAT test campaign: from the turbulence grid to the far-field microphone location. These simulations were performed at the approach condition with the weakly compressible version of the ProLB solver. However, to reach a higher inflow (cutback operating point at roughly M=0.53), the compressible version was mandatory. At both inflow conditions, LBM simulations favourably compare with reference RANS calculations, which validate weakly compressible and compressible simulations. Moreover, acoustic performance of two serrated designs has been assessed, achieving several decibels of noise reduction. Evolution of the noise reduction with respect to the mean flow has also been discussed, showing a trend consistent with the literature. Although the compressible version of the solver is absolutely required to simulate high-speed flows, the weakly compressible version is very appealing at lower Mach numbers, since less equations need to be solved. Finally, compared to the results obtained by analytical and CAA methods in [14], all the present simulations consider the whole test section that includes the installation effects, the seven-blades and its associated cascade-interaction noise, and the turbulence grid avoiding the homogeneous isotropic turbulence assumption as made in CAA simulations. Moreover, acoustic performances, in terms of noise reduction (ΔPWL), obtained with the weakly compressible LBM simulations have been confirmed by comparison with experimental data in [14].

9. Contact Author Email Address

Please feel free to contact the main author at martin.buszyk@onera.fr for further information.

10. Copyright Statement

The authors confirm that they, and/or their company or organization, hold copyright on all of the original material included in this paper. The authors also confirm that they have obtained permission, from the copyright holder of any third party material included in this paper, to publish it as part of their paper. The authors confirm that they give permission, or have obtained permission from the copyright holder of this paper, for the publication and distribution of this paper as part of the ICAS proceedings or as individual off-prints from the proceedings.

11. Acknowledgements

References

[1] S. Narayanan, P. Chaitanya, S. Haeri, P. Joseph, J. W. Kim, and C. Polacsek. Airfoil noise reductions through leading edge serrations. Physics of Fluids, 27(2):025109, 2015.

[2] Paruchuri Chaitanya, P. Joseph, S. Narayanan, Christina Vanderwel, Jacob Mansel Turner, Jae Wook Kim, and Bharathram Ganapathisubramani. Performance and mechanism of sinusoidal leading edge serrations for the reduction of turbulence–aerofoil interaction noise. Journal of Fluid Mechanics, 818:435 – 464, 2017.

[3] Cyril Polacsek, Adil Cader, Martin Buszyk, Raphaël Barrier, Fernando Gea-Aguilera, and Hélène Posson. Aeroacoustic Design and Broadband Noise Predictions of a Fan Stage with Serrated Outlet Guide Vanes. Physics of Fluids, 32(10), October 2020.

[4] Lorna Ayton and Chaitanya Paruchuri. An analytical and experimental investigation of aerofoil-turbulence interaction noise for plates with spanwise-varying leading edges. Journal of Fluid Mechanics, 865:137– 168, 04 2019.

[5] Georgios Bampanis, Michel Roger, Daniele Ragni, Francesco Avallone, and Christopher Teruna. Airfoil-turbulence interaction noise source identification and its reduction by means of leading edge serrations. In 25th AIAA/CEAS Aeroacoustics Conference, 2019.

[6] Martin Buszyk, Cyril Polacsek, and Thomas Le Garrec. Assessment of a CAA methodology for turbulence-cascade interaction noise prediction and reduction from serrated airfoils. In Forum Acusticum 2020, lyon, France, July 2020.

[7] Martin Buszyk, Cyril Polacsek, Thomas Le Garrec, Raphaël Barrier, and Christophe Bailly. Numerical assessment of turbulence-cascade noise reduction and aerodynamic penalties from serrations. AIAA Journal, 0(0):1–17, 0.

[8] Martin Buszyk, Thomas Le Garrec, Cyril Polacsek, and Raphaël Barrier. Lattice Boltzmann simulations in a rectilinear cascade configuration for the turbulence-airfoil interaction noise evaluation and reduction through serrated leading edges. In EURONOISE 2021, Virtuel, Portugal, October 2021.

[9] Prolb: a lattice Boltzmann solver, www.prolb-cfd.com.

[10] Thomas Hainaut, Thomas Le Garrec, Cyril Polacsek, Daniel C. Mincu, and Sebastien Deck. Aerodynamic and aeroacoustic numerical investigation of an axial fan using lattice Boltzmann methods. In 2018 AIAA/CEAS Aeroacoustics Conference, 2018.

[11] Majd Daroukh, Thomas Le Garrec, and Cyril Polacsek. Low-speed turbofan aerodynamic and acoustic prediction with an isothermal lattice Boltzmann method. AIAA Journal, 60(2):1152–1170, 2022.

[12] Damiano Casalino, Francesco Avallone, Ignacio Gonzalez-Martino, and Daniele Ragni. Aeroacoustic study of a wavy stator leading edge in a realistic fan/OGV stage. In 17th International Symposium on Transport Phenomena and Dynamics of Rotating Machinery (ISROMAC2017), Maui, United States, December 2017.

[13] Christopher Teruna, Francesco Avallone, Damiano Casalino, and Daniele Ragni. Numerical investigation of leading edge noise reduction on a rod-airfoil configuration using porous materials and serrations. Journal of Sound and Vibration, 494:115880, 2021.

[14] Cyril Polacsek, Martin Buszyk, Raphaël Barrier, Vincent Clair, and Edouard Salze. Aeroacoustic performances of a low-noise airfoil cascade with serrated leading edges: predictions and measurements. In ICAS 2022 (submitted), 2022.

[15] Jérôme Jacob, Orestis Malaspinas, and Pierre Sagaut. A new hybrid recursive regularised Bhatnagar–Gross–Krook collision model for lattice Boltzmann method-based large eddy simulation. Journal of Turbulence, pages 1 – 26, November 2018.

[16] Thomas Astoul, Gauthier Wissocq, Jean-François Boussuge, Alois Sengissen, and Pierre Sagaut. Analysis and reduction of spurious noise generated at grid refinement interfaces with the lattice Boltzmann method. Journal of Computational Physics, 418:109645, 2020.

[17] Thomas Astoul, Gauthier Wissocq, Jean-François Boussuge, Alois Sengissen, and Pierre Sagaut. Lattice Boltzmann method for computational aeroacoustics on non-uniform meshes: A direct grid coupling approach. Journal of Computational Physics, 447:110667, December 2021.

[18] Emmanuel Lévêque, F. Toschi, Liang Shao, and Jean-Pierre Bertoglio. Shear-improved Smagorinsky model for large-eddy simulation of wall-bounded turbulent flows. Journal of Fluid Mechanics, 570:491–502, 2007.

[19] Florian Renard, Yongliang Feng, Jean-François Boussuge, and Pierre Sagaut. Improved compressible hybrid lattice Boltzmann method on standard lattice for subsonic and supersonic flows. Computers & Fluids, 219:104867, April 2021.

[20] G. Farag, T. Coratger, G. Wissocq, S. Zhao, P. Boivin, and P. Sagaut. A unified hybrid lattice-Boltzmann method for compressible flows: Bridging between pressure-based and density-based methods. Physics of Fluids, 33(8):086101, August 2021.

[21] P.E. Roach. The generation of nearly isotropic turbulence by means of grids. International Journal of Heat and Fluid Flow, 8(2):82–92, 1987.

[22] Danny Lewis. From analytical to fully numerical predictions of the broadband noise radiated by a full fan-OGV stage. Theses, Université de Lyon, November 2020.

[23] Chaitanya Paruchuri. Aerofoil geometry effects on turbulence interaction noise. PhD thesis, University of Southampton, April 2017.

[24] Fernando Gea-Aguilera, James Gill, David Angland, and Xin Zhang. Wavy leading edge airfoils interacting with anisotropic turbulence. In 23rd AIAA/CEAS Aeroacoustics Conference, 06 2017.